

# Determination of scattering coefficient and scattering anisotropy factor of tissue-mimicking phantoms using line-field confocal optical coherence tomography (LC-OCT)

Léna Waszczuk<sup>1,2,\*</sup>, Jonas Ogien<sup>2</sup>, Frédéric Pain<sup>1</sup>, and Arnaud Dubois<sup>1,2</sup>

<sup>1</sup> Université Paris-Saclay, Institut d'Optique Graduate School, CNRS, Laboratoire Charles Fabry, Palaiseau 91127, France

<sup>2</sup> DAMAE Medical, Paris 75013, France

Received 30 May 2023 / Accepted 29 August 2023

**Abstract.** Line-field Confocal Optical Coherence Tomography (LC-OCT) is an imaging modality based on a combination of time-domain optical coherence tomography and reflectance confocal microscopy. LC-OCT provides three-dimensional images of semi-transparent samples with a spatial resolution of  $\sim 1 \mu\text{m}$ . The technique is primarily applied to *in vivo* skin imaging. The image contrast in LC-OCT arises from the backscattering of incident light by the sample microstructures, which is determined by the optical scattering properties of the sample, characterized by the scattering coefficient  $\mu_s$  and the scattering anisotropy factor  $g$ . In biological tissues, the scattering properties are determined by the organization, structure and refractive indexes of the sample. The measurement of these properties using LC-OCT would therefore allow a quantitative characterization of tissues *in vivo*. We present a method for extracting the two scattering properties  $\mu_s$  and  $g$  of tissue-mimicking phantoms from 3D LC-OCT images. The method provides the mean values of  $\mu_s$  and  $g$  over a lateral field of view of  $1.2 \text{ mm} \times 0.5 \text{ mm}$  ( $x \times y$ ). It can be applied to monolayered and bilayered samples, where it allows extraction of  $\mu_s$  and  $g$  of each layer. Our approach is based on a calibration using a phantom with known optical scattering properties and on the application of a theoretical model to the intensity depth profiles acquired by LC-OCT. It was experimentally tested against integrating spheres and collimated transmission measurements for a set of monolayered and bilayered scattering phantoms.

**Keywords:** Line-field confocal optical coherence tomography, Optical coherence tomography, Reflectance confocal microscopy, Optical properties, Scattering.

## 1 Introduction

Line-field Confocal Optical Coherence Tomography (LC-OCT) is a recently introduced optical imaging technique combining the principles of time-domain OCT and reflectance confocal microscopy (RCM) with line illumination and line detection using broadband near infrared light. LC-OCT performs two dimensional (2D) and three-dimensional (3D) imaging with a quasi-isotropic resolution of  $\sim 1 \mu\text{m}$  [1–4]. Up to now, LC-OCT has been applied to skin imaging for healthy skin characterization [5, 6] and early detection and diagnosis of various skin diseases including skin cancers [7–10]. LC-OCT provides images with cellular resolution similar to histology, while being non-invasive.

As in OCT and RCM, the contrast of LC-OCT images originates from the backscattering of light, due to refractive index inhomogeneities within the sample. The amount of

detected backscattered light is determined by three main optical parameters specific to the imaged sample [11]: the absorption coefficient  $\mu_a$ , the scattering coefficient  $\mu_s$ , and the scattering anisotropy factor  $g$ .  $\mu_s$  and  $\mu_a$  correspond to the probability per unit of distance of absorption or scattering events respectively and thus reflect the amount of absorbed and scattered light.  $g$  is defined as the average of the scattering angles cosines along the photon path and hence characterizes the directivity of the scattered light. These optical parameters rule the decay of the OCT image intensity with depth  $I(z)$ , commonly described by a Beer-Lambert law in the single-scattering regime [12]:

$$I(z) \propto \exp(-2\mu z) \quad (1)$$

where  $\mu = \mu_a + \mu_s$  is the attenuation coefficient, characterizing the attenuation of the incident light during in-depth propagation, due to absorption and scattering.

\* Corresponding author: [lena.waszczuk@universite-paris-saclay.fr](mailto:lena.waszczuk@universite-paris-saclay.fr)

The factor 2 accounts for round-trip propagation of light in the sample.

Beyond morphological information, LC-OCT images contain information on optical properties of the sample. Those optical properties are determined by the size, shape and density of tissue light scatterers (nucleus, mitochondria, cytoskeleton, extracellular fiber such as collagen) at cellular and sub-cellular levels. The extraction of optical properties would thus allow access to quantitative information complementary to the morphological information provided by the LC-OCT images. Optical properties could be used as a tool for tissue characterization and quantification of tissue structural changes, which could for instance occur during the development of a pathology.

Quantification of the attenuation coefficient  $\mu$  using conventional OCT has been used for several biomedical applications, such as atherosclerosis plaque characterization [13], human brain cancer infiltration detection [14], glaucoma diagnosis [15], urothelial carcinoma staging and grading [16] or basal cell carcinoma characterization and subtypes differentiation [17]. Several methods have been developed to measure the attenuation coefficient  $\mu$ , as reviewed by [12, 18]. The most common approach is to fit an exponential decay curve on the OCT image intensity as a function of depth to extract the attenuation coefficient  $\mu$ . More recently, Vermeer *et al.* [19] introduced a new method for depth-resolved measurement of the attenuation coefficient. Based on two assumptions (the incident light is completely attenuated within the OCT imaging depth range and the backscattered light is a fixed fraction of the attenuated light), their approach provides a pixel-by-pixel estimation of  $\mu$ , thereby producing attenuation maps with the spatial resolution of the OCT image.

In contrast, fewer work has been reported on the separate measurement of the optical parameters  $\mu_a$ ,  $\mu_s$  and  $g$  using OCT. However, the interest in measuring the optical properties, and especially the scattering parameters  $\mu_s$  and  $g$ , is that each of them provides different and complementary information on tissue structure.  $\mu_s$  is determined by several factors, including the density, size and shape of the scattering particles, while  $g$  is defined by the size and shape of these particles [20]. The measurement of both parameters  $\mu_s$  and  $g$  could therefore provide a comprehensive insight into tissue structural changes occurring in pathologies. The depth-resolved method is limited to the measurement of the attenuation coefficient  $\mu$  due to its assumption that the backscattered light is a fixed fraction of the attenuated light.

A few methods based on curve-fitting allow the measurement of the optical properties  $\mu_a$ ,  $\mu_s$  and  $g$ . Thrane *et al.* [21] introduced a model to extract the optical parameters  $\mu_a$ ,  $\mu_s$  and  $g$  from the OCT image intensity with depth  $I(z)$ . This approach consists in fitting a theoretical model on  $I(z)$ , based on the extended Huygens–Fresnel (EHF) principle. This model was later applied to the skin to distinguish between biopsies of melanoma and benign nevi [22]. In this study, the different layers of skin have not been dissociated and the skin was considered as a monolayered tissue. Studies have been carried out to show the applicability to bilayered samples, however the model becomes cumbersome to

implement [23]. Another simpler approach for extracting the optical properties from OCT images was introduced by Jacques *et al.* [24]. The authors proposed to extract the scattering properties  $\mu_s$  and  $g$  from OCT images using a linear fit. The model, based on Monte-Carlo simulations, was designed for OCT in focus-tracking mode and RCM. It was validated on phantoms with known optical properties [25] and later applied to the extraction of scattering properties of various biological tissues including the skin [26, 27]. This model was also applied on bilayered tissues [28].

As a combination of RCM and OCT (in focus-tracking mode as will be described later), LC-OCT is particularly suitable for the application of the model developed by Jacques *et al.* [24]. Based on this model, we present a method to determine both  $\mu_s$  and  $g$  from LC-OCT images of tissue-mimicking phantoms. Our approach provides the mean values of  $\mu_s$  and  $g$  over a lateral field of view of  $1.2 \text{ mm} \times 0.5 \text{ mm}$  ( $x \times y$ ). It can be applied to monolayered and bilayered samples, where it allows extraction of  $\mu_s$  and  $g$  of each layer. The method was experimentally validated against integrating spheres and collimated transmission measurements on a set of nine monolayered phantoms and two bilayered with distinct optical properties in terms of both scattering properties  $\mu_s$  and  $g$ . The phantoms were made of a polydimethylsiloxane (PDMS) polymer including different types of scattering particles and aim at mimicking tissue scattering properties in the near infrared range. The developed method is simple to implement since it relies on a linear fit and a calibration using one of the fabricated phantoms whose scattering properties were determined by integrating spheres and collimated transmission. The method provides additional quantitative bulk information (*i.e.*, at a macroscopic scale), complementary to LC-OCT images providing information at a microscopic scale.

## 2 Materials and methods

### 2.1 Scattering phantoms

In order to mimic optical properties of biological tissues such as skin [29–31], phantoms were designed with a scattering coefficient  $\mu_s$  ranging from  $\sim 2$  to  $20 \text{ mm}^{-1}$  and an anisotropy factor  $g$  from  $\sim 0.6$  to 1. Since most biological tissues have negligible absorption compared to scattering (scattering is 10–100 times higher than absorption in the near infrared spectrum [29]), we chose  $\mu_a \ll \mu_s$ . In the following, we focus on the measurement of the scattering properties  $\mu_s$  and  $g$ , neglecting the role of  $\mu_a$ .

The phantoms are composed of a PDMS matrix (Sylgard 184 silicone Elastomer Kit, Neyco, France) with a refractive index of 1.42 at the wavelength of 800 nm [32, 33]. To create phantoms with various optical scattering properties, different micro- and nano-powders were added into the PDMS matrix: titanium dioxide ( $\text{TiO}_2$ ) powder (Sigma-Aldrich Corporation, USA), zinc oxide ( $\text{ZnO}$ ) powder (US Research Nanomaterials, Inc., USA) and silicon dioxide ( $\text{SiO}_2$ ) powder (US Research Nanomaterials, Inc., USA). All powders have negligible absorption compared to scattering in the near infrared.

**Table 1.** Summary of monolayered phantoms composition. All phantoms are made of a PDMS matrix including scattering particles of different materials, sizes and concentrations.

Phantom	Particle material	Refractive index	Size	Density (% weight of PDMS)	$\mu_s$ target	$g$ target
No. 0	TiO <sub>2</sub>	2.29	<5 $\mu\text{m}$	0.40%		
No. 1	TiO <sub>2</sub>	2.29	800 nm	0.13%	1.8 $\text{mm}^{-1}$	0.6
No. 2	TiO <sub>2</sub>	2.29	<5 $\mu\text{m}$	0.30%		
No. 3	TiO <sub>2</sub>	2.29	800 nm	1.34%	18 $\text{mm}^{-1}$	0.6
No. 4	ZnO	1.96	800 nm	0.12%	1.4 $\text{mm}^{-1}$	0.8
No. 5	ZnO	1.96	800 nm	1.19%	14 $\text{mm}^{-1}$	0.8
No. 6	SiO <sub>2</sub>	1.54	400 nm	1.27%	1 $\text{mm}^{-1}$	0.7
No. 7	SiO <sub>2</sub>	1.54	400 nm	12.7%	10 $\text{mm}^{-1}$	0.7
No. 8	SiO <sub>2</sub>	1.54	1 $\mu\text{m}$	0.38%	1 $\text{mm}^{-1}$	0.9
No. 9	SiO <sub>2</sub>	1.54	1 $\mu\text{m}$	3.81%	10 $\text{mm}^{-1}$	0.9

**Table 2.** Summary of bilayered phantoms composition, given by the material, size and weight concentration of the scattering particles embedded in PDMS.

Bilayered phantom	phantom Layer	Corresponding monolayered phantom	Particle material	Size	Density (% weight of PDMS)
No. 1	Top layer	Phantom no. 5	ZnO	800 nm	1.19%
	Bottom layer	Phantom no. 2	TiO <sub>2</sub>	<5 $\mu\text{m}$	0.30%
No. 2	Top layer	Phantom no. 2	TiO <sub>2</sub>	<5 $\mu\text{m}$	0.30%
	Bottom layer	Phantom no. 5	ZnO	800 nm	1.19%

In order to select the appropriate scatterers to mimic optical properties of the skin, Mie theory (assuming spherical particles) was used to simulate  $\mu_s$  and  $g$  values of the phantoms as a function of the refractive index, size and density of the particles embedded in PDMS. However, all the parameters necessary to predict the optical properties by Mie theory were not precisely known. For example, only the mean particle size was sometimes given by the manufacturer, without information on the size distribution. The refractive index of the nanoparticles was not provided either. For ZnO and SiO<sub>2</sub> particles, we approximated the refractive index by optical index values extracted from the literature at the 800 nm wavelength [34, 35]. For TiO<sub>2</sub> particles, a wide range of refractive indices was found [34, 36, 37], so an average of the different refractive indices reported in the literature was chosen. Ten different phantoms were fabricated. The detailed description of the composition of the phantoms is given in Table 1, with target values of  $\mu_s$  and  $g$  computed using Mie theory when possible. The target values of  $\mu_s$  and  $g$  are not given for phantoms 0 and 3 due to the lack of precise information on the size of the particles used (<5  $\mu\text{m}$ ).

The PDMS matrix was fabricated using a ratio of 10:1 by weight of PDMS pre-polymer and curing agent. All phantoms were prepared by first mixing the curing agent with a variable amount of scattering powder. The mixture

was placed in an ultrasonic bath for 30 min to prevent particles aggregation, and then mixed with the PDMS pre-polymer. The obtained mixture was poured on a 40-mm diameter petri dish. The volume poured was chosen in order to obtain 1–2.5 mm thick phantoms, a thickness allowing their characterization by integrating spheres. Air bubbles were removed using a vacuum pump for 1 h, and the phantom mixture was finally cured for 1 1/2 h at 80 °C.

We also designed two bilayered phantoms with distinct optical properties in each layer, as listed in Table 2. To create the top layer, a small volume of the PDMS/scattering powder mixture was poured in a petri dish. The phantom was left for 24 h in a vacuum chamber at room temperature, allowing the mixture to spread into a thin layer before curing. This process allows to achieve a thickness of ~100  $\mu\text{m}$ . Since this phantom is very fragile, another thicker phantom was fabricated using the same batch mixture, facilitating the measurement of the top layer scattering properties using integrating spheres and collimated transmission setup. Once cured, the obtained top layer was stacked on a thicker phantom with different optical properties to create a bilayered phantom, using a small drop of paraffin oil (refractive index of ~1.47) between the two layers for optical contact. A representative LC-OCT image corresponding to a vertical image (*i.e.*, cross-sectional view) of one of the bilayered phantoms is shown in Figure 1.

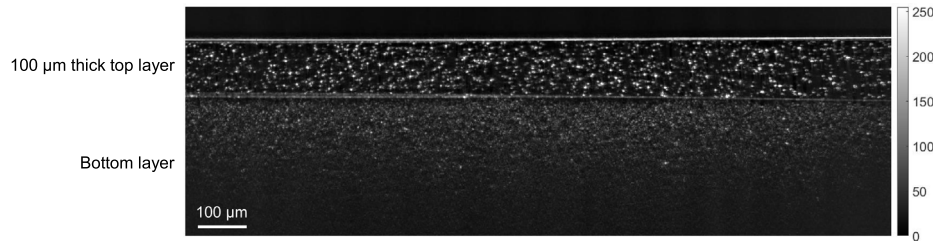


**Figure 1.** LC-OCT vertical image (*i.e.*, cross-sectional view) of a bilayered phantom. The LC-OCT image is displayed in a logarithmic intensity scale (arbitrary unit).

## 2.2 Integrating spheres and collimated transmission measurements

Mie theory allows to define target values for  $\mu_s$  and  $g$ . However, as previously mentioned, the characterization of the optical properties by Mie theory is not very reliable due to uncertainties on the size distribution and the refractive indices of the particles used in our phantoms. Therefore, these target values are indicative values but cannot be used as reference values to compare with values obtained from LC-OCT images. Thus, the optical properties of our samples were characterized experimentally, using integrating spheres and collimated transmission devices.

Integrating spheres measurement is a common method to measure optical properties of samples [38–40]. It consists in measuring the diffuse reflectance and diffuse transmittance of a sample using a set-up with one or two hollow spheres with a diffuse reflective internal coating. The absorption coefficient  $\mu_a$  and the reduced scattering coefficient  $\mu'_s = \mu_s(1 - g)$  are then derived from these two measurements using theoretical models [41]. In order to separate the reduced scattering coefficient  $\mu'_s$  into the scattering coefficient  $\mu_s$  and the scattering anisotropy factor  $g$ , a collimated transmission measurement is required. This measurement is obtained by collecting the ballistic light from a laser beam propagating perpendicularly to the phantom. A more detailed description of integrating spheres and collimated transmission measurements can be found in [42].

We used a set-up with two integrating spheres (2" Integrating Sphere IS200-4, Thorlabs, USA). The sample was placed between the two spheres. Light from a high-power broadband Xenon light source (HPX 2000, Ocean Insight, Dunedin, Florida) was guided to one of the two spheres using a 50/125 optical fiber and collimated into a 6-mm diameter beam. Diffuse reflected and transmitted light were collected using an optical fiber (plastic fiber, PMMA Toray, 50-cm long, 1-mm diameter, 0.22 NA) coupled to a spectrometer (AvaSpec2048, Avantes, Netherlands). Collimated transmission measurement was carried out with a monochromatic fiber laser diode at 785 nm (Micron Cheeta, Sacher LaserTechnik, Germany). The laser beam was collimated at the fiber output and its diameter was reduced using a diaphragm. The phantom was placed a few cm behind the diaphragm, perpendicular to the laser beam. A collection fiber (105  $\mu\text{m}$  core diameter, 0.1 NA), connected to the spectrometer, was placed one meter behind the phantom in order to collect the ballistic light. Due to its small diameter, low numerical aperture and large distance to

the sample, the fiber acts as a pinhole rejecting scattered photons.

All measurements were corrected for dark noise and normalized with respect to blank measurements without sample. The optical properties were computed using the Inverse Adding-Doubling (IAD) algorithm developed by Prahl [43].  $\mu_s$  and  $g$  were determined at the wavelength of 785 nm. Despite the slight difference in wavelength from that of the LC-OCT device centered at 800 nm, the difference in  $\mu_s$  and  $g$  values between these two wavelengths can be considered negligible compared to the accuracy of our measurements [39], allowing for comparison of integrating spheres and collimated transmission measurements with measurements obtained from LC-OCT images.

In practice, the collimated transmission measurement could not be performed on some of the highly concentrated phantoms (3, 5, 7 and 9) since the ballistic intensity was too weak. However, phantoms 3, 5, 7 and 9 are made of the same scattering particles as phantoms 1, 4, 6 and 8 respectively. Since  $g$  is ruled by particle size and shape [20], the values of  $g$  of phantoms 3, 5, 7 and 9 were considered identical to those of phantoms 1, 4, 6 and 8 respectively.

For bilayered phantoms, the top and bottom layers were analyzed separately since integrating spheres and collimated transmission do not allow to separate the scattering properties of two stacked layers. As previously mentioned, since the 100  $\mu\text{m}$ -thick top layer was very fragile, the scattering properties of the top layer were measured on a thicker phantom fabricated with the same batch mixture as the thin top layer.

## 2.3 LC-OCT measurements

### 2.3.1 LC-OCT device

The LC-OCT device used in this work is described in [1–4]. The device is based on a Linnik interferometer with a 0.5 NA water-immersion microscope objective in each arm. A supercontinuum light source centered around 800 nm is used to generate spatially coherent ultra-broadband light. Line illumination of the sample is achieved using a cylindrical lens, and backscattered light is detected with a line camera. LC-OCT is capable of generating 2D vertical section images (*i.e.*, cross-sectional views,  $x \times z$ ) and horizontal section images (*i.e.*, *en-face* views,  $x \times y$ ). By combining the depth and lateral scans used to generate 2D images, 3D images can also be obtained, with a quasi-isotropic resolution of  $\sim 1 \mu\text{m}$  over a field of view of

1.2 mm  $\times$  0.5 mm  $\times$  0.5 mm ( $x \times y \times z$ ). During imaging, samples are placed in contact with a glass plate to stabilize them and maintain them at the position corresponding to the working distance of the microscope objective. Paraffin oil is placed between the phantoms and the glass plate to minimize parasitic reflections at the interface.

### 2.3.2 Theoretical model for measuring $\mu_s$ and $g$

Within the single-scattering regime and in focus-tracking mode, the reflectance  $R(z)$  measured along an A-scan acquired by OCT or LC-OCT image (*i.e.*, the depth-dependent fraction of incident light backscattered and collected by the device) can be described by an exponential decay with depth [29]:

$$R(z) = \rho \exp(-2\mu z). \quad (2)$$

$\rho$  is the fraction of light backscattered at the focus into the collection solid angle of the LC-OCT microscope objective;  $\mu = \mu_s + \mu_a$  is the attenuation coefficient previously introduced, and the factor 2 accounts for round-trip attenuation inside the sample. Since the factor  $1/\mu_s$  represents the average distance between two scattering events [44], the single scattering regime is valid as long as  $\mu_s z \leq 1$ . This model of the LC-OCT signal is therefore valid for media with low scattering properties or/and at shallow penetration depths. In order to be able to measure the optical properties of more scattering media, Jacques *et al.* [29] proposed a model, also based on an exponential decay law, allowing to take into account forward directed multiple scattering:

$$R(z) = \rho \exp(-2\mu_{\text{eff}} z), \quad (3)$$

where

$$\begin{cases} \mu_{\text{eff}} = G(g, \text{NA})(\mu_a + a(g)\mu_s) \\ \rho = \mu_s \Delta z b(g, \text{NA}) \end{cases}, \quad (4)$$

where  $G(\text{NA}, g)$ ,  $a(g)$  and  $b(g, \text{NA})$  are model parameters described in [24] and  $\Delta z$  the axial resolution of the imaging device. Note that in the case of RCM, the authors mention that a corrective factor may be necessary to account for a difference between the theoretical axial resolution of the RCM system and the effective axial resolution to be taken into account in the model [28]. In the case of LC-OCT, the axial resolution was computed as  $\Delta Z = \frac{2 \log(2)}{\pi} \frac{\lambda^2}{\Delta \lambda} = 1.2 \mu\text{m}$  and no corrective factor was required based on results presented later in this paper.

$G(\text{NA}, g)$  describes the average optical path length traveled by the photons collected by the OCT system, taking into account the numerical aperture NA and the scattering anisotropy factor  $g$  of the imaged sample. This term takes into account the fact that photons emitted at the edge of the beam travel a longer optical path than photons emitted on the optical axis. For NA = 0.5 (numerical aperture of the LC-OCT device),  $G$  is close to 1 [24].

$a(g)$  is called the scattering efficiency factor. It reflects the contribution of forward scattered photons, *i.e.*, serpentine photons. Serpentine photons can contribute to the

backscattered intensity because of their trajectory similar to that of ballistic photons. Then, if they follow a serpentine trajectory on the return path, photons can contribute to the collected intensity. Thus, serpentine photons slow down the extinction of the incident intensity by scattering in the sample. This effect has been formalized in the form of a function  $a(g)$ :

$$a(g) \approx u(1 - e^{-(1-g)^v/w}). \quad (5)$$

with  $u$ ,  $v$ , and  $w$  parameters determined by Monte-Carlo simulations [24, 26]. For small values of  $g$  (isotropic scattering medium),  $a(g)$  is close to 1, which implies that  $\mu_{\text{eff}} = \mu$  as in the single-scattering regime. However, for values of  $g$  tending towards 1 (highly forward scattering medium),  $a(g)$  tends towards 0, leading  $\mu_{\text{eff}} < \mu$ , meaning that attenuation of light is slowed down by the contribution of serpentine photons. The authors have shown that this modeling of the contribution of multiple forward scattered photons is valid as long as  $\mu_s z \leq 3$  [25]. However, this modeling does not take into account the possible contribution of photons multiply scattered along a non-ballistic optical path. This typically allows the measurement of scattering coefficients on the order of  $10 \text{ mm}^{-1}$  down to a depth of 400  $\mu\text{m}$ , and down to 200  $\mu\text{m}$  for the most scattering phantoms (up to  $20 \text{ mm}^{-1}$ ). Jacques' model thus appears to be very well adapted to the measurement of optical properties of biological tissues imaged with LC-OCT.

$b(g, \text{NA})$  is qualified as collection efficiency and represents the fraction of light scattered from probed volume and collected by the microscope objective of the LC-OCT device.  $b(g, \text{NA})$  is ruled by the phase function of the sample, described by the Henyey–Greenstein function in this model [45], and the collection angle of the microscope objective, given by the value of NA.

In this modeling of  $R(z)$ ,  $\rho$  and  $\mu_{\text{eff}}$  can be considered as experimental observables and can be extracted from an LC-OCT image as described in the following section.

### 2.3.3 Processing of LC-OCT images for extracting $\mu_s$ and $g$ on monolayered phantoms

The principle of our method consists in measuring  $\mu_{\text{eff}}$  and  $\rho$  parameters from an LC-OCT image, and to convert these parameters into the optical properties  $\mu_s$  and  $g$  using the previously described model proposed by Jacques *et al.* To do so, a 3D LC-OCT image is acquired for each phantom. The 3D image results from the acquisition of a stack of 2D LC-OCT horizontal images (*i.e.*, *en-face* sections). Each image of the stack is obtained by demodulating the interferometric lines acquired successively in the horizontal plane during the lateral scan, using a phase-shifting algorithm [4]. No processing is applied to the LC-OCT images in order not to distort the measurement of the scattering properties. The first step is to compute the reflectance  $R(z)$ . Since phantoms have a homogeneous distribution of scattering particles, the mean reflectance  $R(z)$  in the 3D image is considered. All A-scans within the 3D LC-OCT image are averaged to obtain a mean depth-dependent intensity  $I(z)$ . Since the phantoms are composed of discrete scattering particles,

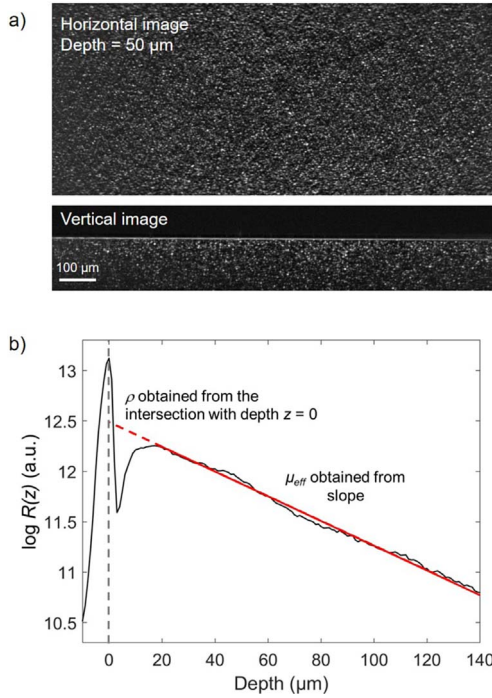


**Figure 2.** (a) 3D LC-OCT image (horizontal or en face view and vertical or cross-sectional view) of a phantom made of PDMS and TiO<sub>2</sub> particles, in logarithmic intensity scale and (b) averaged intensity profile  $I(z)$  in the 3D LCOCT image as a function of depth, in logarithmic scale. A linear regression (red line) is applied on the intensity profile to obtain the measurement of the pair of observables  $\mu_{\text{eff}}$  and  $\rho$ .

averaging all A-scans within the 3D image provides the smoothest possible intensity profile  $I(z)$ , which will then help maximize the quality of the linear regression that will be applied as described in the following. The mean reflectance  $R(z)$  is then obtained by converting  $I(z)$  into dimensionless units of reflectance using a calibration constant  $f$ :  $R(z) = fI(z)$ . This simple calibration using a proportionality factor is made possible since LC-OCT operates in focus-tracking mode and thus does not require confocal functions to be taken into account as is sometimes the case with conventional OCT [12, 18].

$\rho$  and  $\mu_{\text{eff}}$  are extracted by applying a least square linear regression on  $\log R(z)$  (Fig. 2), from the surface of the sample down to a depth of about 150  $\mu\text{m}$ .  $\rho$  is obtained from  $\log \rho$ , which corresponds to the intercept with depth  $z = 0$  representing the interface between the glass plate and the phantom (intensity peak visible at  $z = 0$  in Fig. 2);  $\mu_{\text{eff}}$  is given by half the slope of the linear regression.

Finally, the resulting parameters  $\rho$  and  $\mu_{\text{eff}}$  extracted from the 3D LC-OCT image are mapped to the optical properties  $\mu_s$  and  $g$  using the model by Jacques *et al.* previously described. Several ways can be considered to recover  $\mu_s$  and  $g$  from  $\mu_{\text{eff}}$  and  $\rho$  using equations (4) of the Jacques' model. In this paper, the following relationship was used considering  $\mu_a \ll \mu_s$ :

$$\frac{\mu_{\text{eff}}}{\rho} = \frac{aG}{b\Delta z}. \quad (6)$$

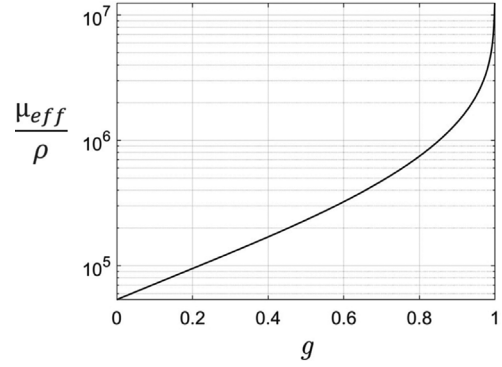


**Figure 3.** Ratio of  $\mu_{\text{eff}}/\rho$  as a function of  $g$ , calculated for  $\lambda = 800$  nm, NA = 0.5 and  $\Delta z = 1.2$   $\mu\text{m}$ .

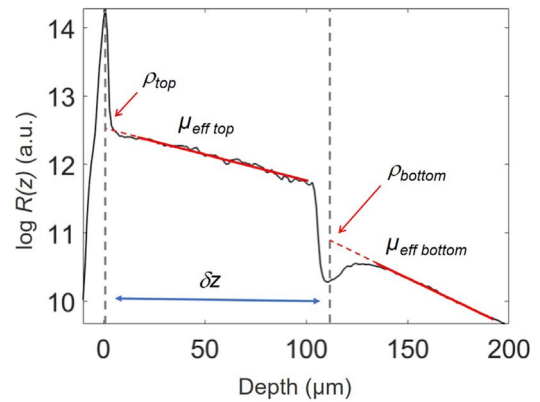


**Figure 4.** Averaged intensity profile  $R(z)$  in the 3D LC-OCT image of a bilayered phantom as a function of depth (in logarithmic scale). For each layer, a linear regression (red line) is applied on the intensity profile to obtain the measurement of the pair of observables ( $\rho_{\text{top}}$ ,  $\mu_{\text{top}}$ ) and ( $\rho_{\text{bottom}}$ ,  $\mu_{\text{bottom}}$ ). The value of  $\rho_{\text{bottom}}$  is retrieved from the intercept with the interface between the two layers ( $z = 110$   $\mu\text{m}$ ) corrected from attenuation in the top layer.

The expression of  $\frac{\mu_{\text{eff}}}{\rho}$ , proposed by Jacques *et al.* in [24], is a function of  $\lambda$ , NA and  $g$  and is independent from  $\mu_s$ . The curve  $\frac{\mu_{\text{eff}}}{\rho}$  as a function of  $g$  (for  $\lambda = 800$  nm and NA = 0.5), shown in Figure 3, can thus be used to compute the value of  $g$  from the two observables  $\rho$  and  $\mu_{\text{eff}}$ .  $\mu_s$  can then be recovered from the value of  $\mu_{\text{eff}}$  and  $g$  using equations (4). The resulting  $\mu_s$  and  $g$  values correspond to the mean optical properties over the LC-OCT lateral field of view of 1.2 mm  $\times$  0.5 mm ( $x \times y$ ).

### 2.3.4 Measurements on bilayered phantoms

For bilayered phantoms, two distinct areas of linear decay can be observed on the averaged intensity profile plotted in Figure 4, corresponding to the two layers of the sample. Since the two layers have different optical properties, they exhibit different slopes. As for the monolayered phantoms, the intensity peak at depth  $z = 0$  indicates the interface between the glass slide and the phantom. In this example, the intensity peak around 110  $\mu\text{m}$  depth shows the interface

between the two layers. To extract the values of  $\mu_{\text{eff}}$  and  $\rho$  in each layer (noted  $\rho_{\text{top}}$ ,  $\mu_{\text{efftop}}$  and  $\rho_{\text{bottom}}$ ,  $\mu_{\text{effbottom}}$ ), the two layers are segmented by manually delineating the two areas of linear decay. A linear fit is then applied separately on each layer, as depicted in Figure 4. In the bottom layer, the intercept with the interface between the two layers (at depth  $z = 110 \mu\text{m}$ ) corresponds to  $\log(\rho_{\text{bottom}} e^{-2\mu_{\text{efftop}}\delta z})$  due to attenuation in the top layer of thickness  $\delta z$ .  $\rho_{\text{bottom}}$  is retrieved from  $\rho_{\text{bottom}} e^{-2\mu_{\text{efftop}}\delta z}$  by multiplying it with a correction factor  $C = e^{2\mu_{\text{efftop}}\delta z}$  to compensate from attenuation in the top layer.

The resulting parameters  $\rho_{\text{top}}$ ,  $\mu_{\text{efftop}}$  and  $\rho_{\text{bottom}}$ ,  $\mu_{\text{effbottom}}$  are then mapped to the optical properties  $\mu_s$  and  $g$  in each layer using the model by Jacques *et al.* as described in the previous section.

### 2.3.5 Calibration

As introduced in the previous section, the mean intensity  $I(z)$  (in gray levels) in an LC-OCT image can be converted into dimensionless units of reflectance  $R(z)$  using a calibration constant  $f$  such that  $R(z) = fI(z)$ . To determine  $f$ , one of the phantoms was used as a calibration phantom. On the one hand,  $\mu_s$  and  $g$  of the calibration phantom were obtained from integrating spheres and collimated transmission measurements. Using the model of Jacques *et al.* [24], the ratio  $r_{\text{calib}} = \frac{\mu_{\text{effcalib}}}{\rho_{\text{calib}}}$  was determined from the  $g$  value measured for this phantom. On the other hand, a 3D image of the calibration phantom was acquired. The values of  $I_0\rho_{\text{calib}}$  and  $\mu_{\text{calib}}$  were extracted by applying a linear regression on the mean intensity  $I(z)$  in the image. Knowing the value of the expected  $r_{\text{calib}}$  ratio, the value of  $\rho_{\text{calib}}$  can be obtained from  $\mu_{\text{effcalib}}$ . A calibration factor  $f$  can then be calculated as the ratio of the expected value for  $\rho_{\text{calib}}$  and the value of  $I_0\rho_{\text{calib}}$  measured from the 3D LC-OCT image:

$$f = \frac{\rho_{\text{calib}}}{I_0\rho_{\text{calib}}}. \quad (7)$$

Other calibration approaches can be considered, but this approach has the advantage that it does not involve the value of  $\mu_s$  measured using integrating spheres and collimated transmission. This is an interesting feature: while the value of  $g$  is independent from particle density, this is not the case of  $\mu_s$ . Since integrating spheres and collimated transmission measurements are performed on a field of 6 mm diameter and LC-OCT measurements on a field of the order of 1 mm, it is preferable in case of particle density heterogeneities in the calibration phantom to use only the  $g$  value obtained using integrating spheres and collimated transmission to calibrate reflectance in LC-OCT images.

### 2.4 Evaluation of uncertainties

For each phantom, integrating spheres and collimated transmission measurements were performed three times. Mean values of  $\mu_s$  and  $g$  obtained with integrating spheres and collimated transmission were calculated from these three measurements.

Since LC-OCT measurements are based on a calibration performed with a calibration phantom whose optical properties are obtained by integrating spheres and collimated

transmission measurements, the uncertainties of the integrating spheres and collimated transmission method have a significant impact on the accuracy of LC-OCT measurements of  $\mu_s$  and  $g$ . Values of  $\mu_s$  and  $g$  were computed from mean values of  $\mu_s$  and  $g$  obtained from three 3D LC-OCT image, and uncertainties on LC-OCT measurements were estimated as follows: first, the uncertainty on the calibration factor  $f$  was estimated from uncertainties obtained on  $\mu_s$  and  $g$  values of the calibration phantom measured using integrating spheres and collimated transmission measurements. From the resulting uncertainty on  $f$ , the uncertainty on  $\rho$ , due to calibration, was obtained for each fabricated phantom. Additional uncertainties on  $\rho$  and  $\mu_{\text{eff}}$  were experimentally observed due both to least square linear regression on the intensity depth profile extracted from the 3D image and to slight variations of  $\rho$  and  $\mu_{\text{eff}}$  from one image to another of the same phantom. Finally, uncertainties on  $\mu_s$  and  $g$  were evaluated for each fabricated phantom by propagating total uncertainties on  $\rho$  and  $\mu_{\text{eff}}$  through the model of Jacques [24] previously described.

## 3 Results and discussion

### 3.1 Monolayered phantoms

Comparisons of  $\mu_s$  and  $g$  values of monolayered phantoms obtained from LC-OCT mean intensity depth profiles and integrating spheres and collimated transmission measurements are given in Figures 5 and 6. Additionally, values of  $\mu_a$  obtained from integrating spheres and collimated transmission measurements are given in Figure A1 of Appendix A.

First of all, one can observe that the optical scattering properties obtained correspond to the range of properties targeted, with  $\mu_s$  values between 1 and 25  $\text{mm}^{-1}$  and  $g$  values between 0.68 and 0.94. The obtained results confirm that  $\mu_a \ll \mu_s$  for all phantoms. For phantoms made of the same particles (in terms of refractive index and size), one can notice that the value of  $\mu_s$  increases with the particle concentration, in agreement with Mie theory. The measured values of  $\mu_s$  do not correspond exactly to the theoretical values, but the order of magnitude is similar. As stated earlier, the theoretical values are indicative due to uncertainties in the size and refractive index of the scattering particles. Moreover, it should be noted that during the fabrication process, particle losses may have occurred when pouring the particle/hardener mixture into the prepolymer, which may also contribute to some deviations in  $\mu_s$ . Concerning the  $g$  parameter, we can note that here again the values of  $g$  for the phantoms 1, 4 and 8 have the same order of magnitude compared to Mie theory. However, the value of  $g$  obtained for phantom 6, composed of 400 nm  $\text{SiO}_2$  particles, is largely higher (0.94) than the target value (0.7) and is equivalent to the value of  $g$  obtained for phantom 8, composed of  $\text{SiO}_2$  particles of larger size (1  $\mu\text{m}$ ). A possible explanation could be the aggregation of 400 nm particles into larger particles, of the order of 1  $\mu\text{m}$ .

When looking at the comparison of  $\mu_s$  and  $g$  values between the two measurement methods, results show that, for phantoms 1–6 and 8, LC-OCT is capable of providing

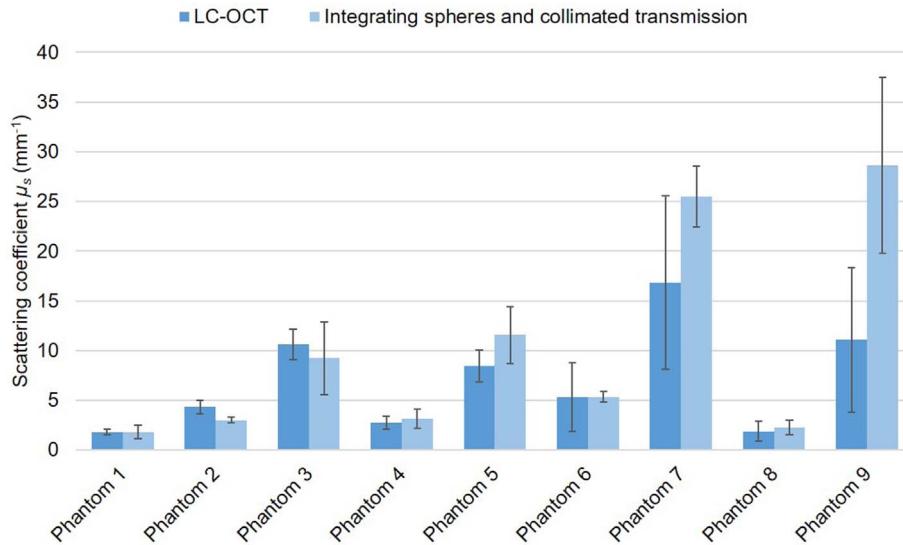


**Figure 5.** Comparison of  $\mu_s$  values obtained by LC-OCT and combined integrating spheres and collimated transmission measurements on monolayered phantoms. Mean values and error bars were determined as explained in detail in [Section 2.4](#).

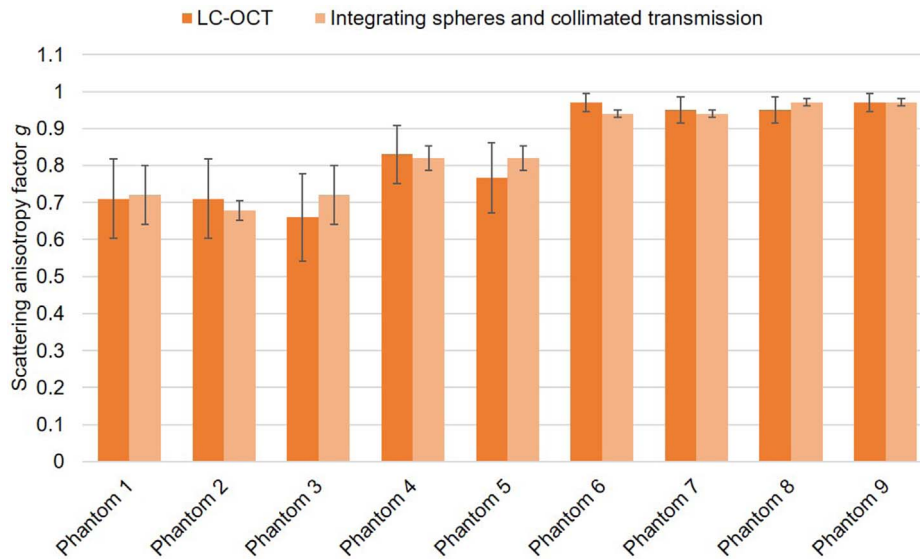


**Figure 6.** Comparison of  $g$  values obtained by LC-OCT and combined integrating spheres and collimated transmission measurements on monolayered phantoms. Mean values and error bars were determined as explained in detail in [Section 2.4](#).

measurements of optical properties consistent with those obtained by integrating spheres and collimated transmission measurements, with overlapping error bars (nearly overlapping for the  $\mu_s$  measurement for phantom 2). For phantoms 7 and 9, one observes a good agreement of  $g$  values between the two methods. On the other hand, we observe a significant discrepancy between the value of  $\mu_s$  measured by integrating spheres and collimated transmission and that measured by LC-OCT. To date, we have no definitive explanation for this discrepancy, but a potential explanation could be the presence of aggregates in phantoms. As shown by high-resolution bright field microscopy images (acquired with a 1.35 NA objective) given in [Figure 7](#), aggregates could be observed in some areas of our phantoms, while other areas were well homogeneous. We

also observed a greater number of aggregates as we penetrated deeper into the phantoms. LC-OCT images covered a  $1.2 \text{ mm} \times 0.5 \text{ mm} \times 0.5 \text{ mm}$  ( $x \times y \times z$ ) field of view, and were acquired in regions excluding aggregates (or at least minimizing their number). In contrast, the integrating spheres and collimated transmission measurements are based on transmission through the entire thickness of the phantom and over a lateral diameter of 6 mm, which potentially takes into account much more aggregates than LC-OCT. This issue shows the limitation of our fabrication process. In the future, it would be necessary to revise the manufacturing process, for instance with better mechanical mixing to improve homogeneity.

The measurements of  $\mu_s$  and  $g$  have fairly high uncertainties, represented by the error bars in [Figures 5 and 6](#).



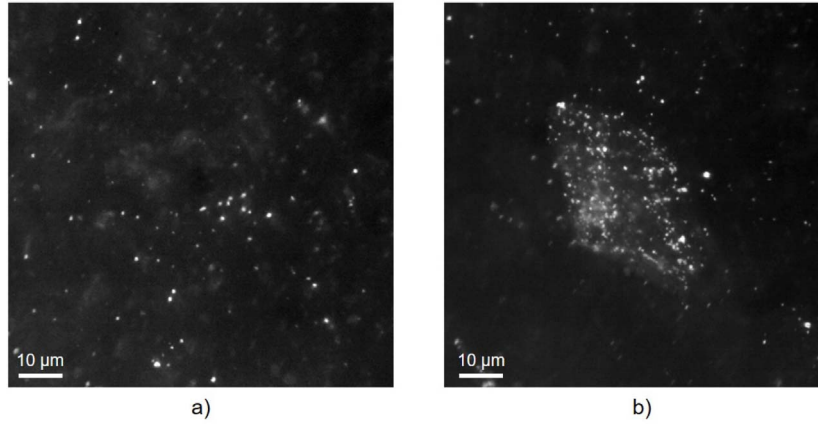


**Figure 7.** High-resolution microscopic images of phantom 9 acquired with a 1.35 NA objective. (a) Image acquired in a homogeneous region without aggregates and (b) image acquired in a region with particle aggregates.

The error bars associated with the integrating spheres and collimated transmission measurements reflect the difficulty to perform these measurements. Indeed, although being a reference method, the collimated transmission measurement is an experimental measurement that was difficult to perform in a repeatable way and that required improvements to the initial setup. In particular, since the phantoms were not perfectly flat, the ballistic beam could be deflected. It was therefore necessary to readjust the injection in the collecting fiber for each phantom. Another potential source of error in the collimated transmission measurement is the contribution of multiple scattered photons to the ballistic intensity when the value of  $g$  is high. The proportion of scattered photons collected compared to ballistic photons depends on the scattering properties and on the acceptance angle of the collection system. In this paper, the contribution of multiple scattering to collimated transmission was minimized at best using a fiber with a small core, low numerical aperture and placed far from the sample allowing to minimize the collection angle. Experimental difficulties lead to uncertainties not only on  $\mu_s$  and  $g$  values determined with integrating spheres and collimated transmission, but also on LC-OCT measurements since the calibration is performed using a phantom with optical properties determined by this method, as explained in Section 2.4. When propagated through the model, these errors are amplified for high values of  $\mu_s$  and  $g$ . This is why the error bars are strongly dependent on the optical properties of the phantoms. Thus, they are the widest for phantoms 6–9 which have a high value of  $g$ .

In summary, despite the issues encountered with phantoms 7 and 9, results obtained show that our measurement method is well suited to samples with medium to high scattering anisotropy ( $0.7 < g < 0.9$ ) and scattering coefficients  $\mu_s$  up to  $12 \text{ mm}^{-1}$ , which already allows for application to biological tissues.

### 3.2 Bilayered phantoms

The results obtained on the bilayered phantoms are shown in Figure 8. The two layers of the bilayered phantoms have very different values of  $\mu_s$  and  $g$ . The results show that for

each layer, LC-OCT provides optical properties that are consistent with those obtained by the integrating spheres and collimated transmission method, with overlapping error bars. A very good agreement of  $g$  values can be observed between the two measurement methods, both for the top and bottom layers of the two bilayer phantoms.

Concerning  $\mu_s$  values, one can also observe a good agreement for all layers. Overall, the difference between the two measurement methods on  $\mu_s$  remains of the same order as the difference obtained on the monolayered phantoms. One can notice that the value of  $\mu_s$  in the bottom layer of the bilayer phantom 2 is slightly lower than the value of  $\mu_s$  obtained with the monolayer phantom 5 alone, a difference that can possibly be explained by a more important contribution of multiple scattering than with the monolayer phantom 5 since the linear regression on the bottom layer is applied deeper (from 100 to 200  $\mu\text{m}$ ). The model of Jacques *et al.* takes into account the multiple scattering in certain extent and when scattering is directed forward. In order to better account for multiple scattering in its entirety, multiple scattering models such as the EHF model proposed by Thrane *et al.* [21] could be used. However, the investigations of the EHF model carried out so far have not been conclusive and have led to unrealistic values of optical properties, an issue that was previously mentioned in [46]. It was suggested in [18] that the model needs a priori knowledge of  $\mu_s$  or  $g$  since they are co-dependent parameters in the model. Moreover, this model is not yet suitable for the application to multilayered samples due to its complexity.

Nevertheless, our results obtained on bilayered phantoms demonstrate the potential of LC-OCT to provide layer-based measurements of distinct  $\mu_s$  and  $g$  values from a single 3D image, unlike the integrating spheres and collimated transmission method which requires the two layers to be analyzed separately. Compared to the current state of the art, the application of our method on bilayered phantoms with different values of  $\mu_s$  and  $g$  in each layer is innovative since previously reported multilayered phantoms have identical  $g$  values in all layers. However, our fabrication process would need to be improved for obtaining a more homogeneous thin top layer. Indeed, as for monolayered phantoms, aggregate deposition in the bottom of the

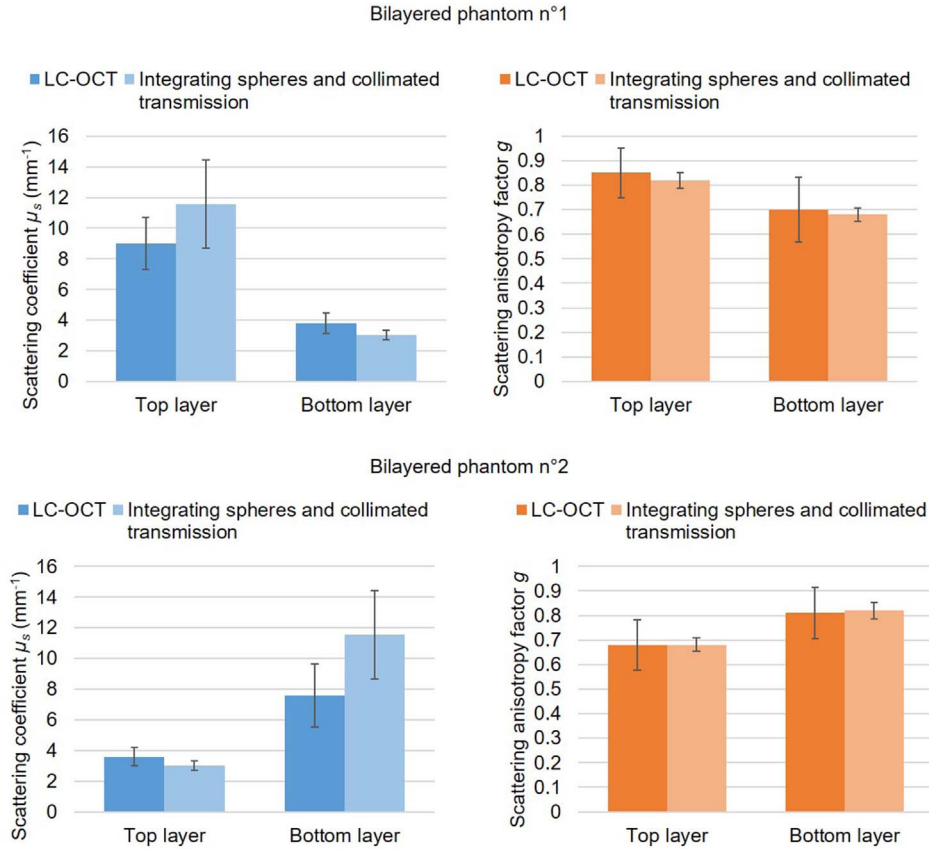


**Figure 8.** Comparison of  $\mu_s$  and  $g$  values (mean  $\pm$  standard deviation) obtained by LC-OCT and combined integrating spheres and collimated transmission measurements on two different bilayered phantoms.

thin layers has sometimes been observed. One solution could be to cut a thin layer from a thicker sample that would be more homogeneous.

## 4 Conclusion and perspectives

We have developed a method for measuring the scattering coefficient  $\mu_s$  and the scattering anisotropy factor  $g$  of a sample from a single 3D image of that sample acquired by LC-OCT. Our approach is based on the extraction of two observables  $\rho$  and  $\mu_{\text{eff}}$  from the LC-OCT image, by applying a linear fit to the mean intensity depth-profile within the 3D image (in logarithmic scale). Using a calibration with a phantom of known optical properties and a model previously introduced in the literature [24], the values of  $\rho$  and  $\mu_{\text{eff}}$  can be mapped to the values of the scattering parameters  $\mu_s$  and  $g$ . We tested our method on PDMS phantoms containing nano- and micro-scattering particles mimicking optical properties of typical biological tissues, and compared it to another commonly used method based on integrating spheres and collimated transmission measurements. The values obtained measured by LC-OCT are consistent with those obtained from the integrating spheres and collimated transmission measurements, suggesting that LC-OCT is a relevant tool to measure the optical scattering properties of semi-transparent samples.

Compared to integrating spheres and collimated transmission measurements that require manipulating the sample (place it between the spheres, then move it on the collimated transmission bench) and involves constraints on the sample physical characteristics (minimum size corresponding to the beam diameter, minimum thickness to be placed between the two spheres without risk of damaging the sample, maximum thickness for the collimated transmission to be possible), LC-OCT does not require specific sample handling and constraints, which simplifies the measurement procedure and would facilitate *in vivo* measurements of  $\mu_s$  and  $g$ . Moreover, LC-OCT allows measurements on multilayered samples with distinct optical properties in each layer, using a single 3D image, unlike integrating spheres and collimated transmission which require analyzing the different layers separately. In this paper, we demonstrate the applicability of our method to bilayered samples, with the ultimate aim of applying the approach to the two main layers of the skin, the epidermis and the dermis. However, our method is not limited to two layers, but could be applied to multilayered samples ( $>2$ ) following the same approach as for bilayered samples, as described in Section 2.3.4.

Our layer-based approach is interesting since few papers have reported measurement by OCT of 1 distinct  $\mu_s$  and  $g$  values on multilayered samples [47, 48]. Compared to these previous works, our developed method has the advantage of

being very simple to implement since it is based on a linear fit and a scattering model, and requires only a preliminary calibration step, using a phantom with known optical properties. Since LC-OCT is based on time-domain OCT with dynamic focusing, LC-OCT measurements do not require corrections accounting for the confocal function of the focusing lens [12]; this is another reason why LC-OCT is particularly appropriate for the application of Jacques' model.

The model of Jacques *et al.* takes into account multiple scattering when scattering is strongly directed forward, but it does not extensively account for multiple scattering as the extended Huygens–Fresnel (EHF) model does [21]. However, investigations of the EHF model have not yet given conclusive results on our phantoms. Moreover, Jacques' model does not account for absorption, which restricts application to purely scattering samples (excluding for instance biological tissues with a high concentration of blood vessels or melanin). Our approach is also limited by the calibration step using a phantom with optical properties determined by integrating spheres and collimated transmission measurements. In particular, the collimated transmission measurement is complex to implement, leading to significant uncertainties of the measurement of  $\mu_s$  and  $g$ , especially for high values of  $\mu_s$  and  $g$ . Other techniques for measuring  $g$  (e.g., goniometry) could be investigated to reduce the uncertainties of collimated transmission measurements. However, goniometry, as collimated transmission, is complex to perform and requires constraints on the geometry of the samples in order to be able to collect scattered intensity from all angles [49].

Since LC-OCT provides morphological images, a future prospect could be to perform spatially resolved measurements of  $\mu_s$  and  $g$  in a horizontal plane, in addition to the layer-based measurements obtained on the bilayered phantoms. Such spatially-resolved measurements could be obtained by dividing the 3D LC-OCT image into macro-voxels, in which values of  $\mu_s$  and  $g$  could be extracted using the mean intensity depth profile in each macro-voxel. A macroscopic spatial distribution of  $\mu_s$  and  $g$  could then be obtained. Further investigation is required to apply our method to biological tissues. LC-OCT is an imaging modality designed for biological tissue imaging, and in particular for skin imaging *in vivo*. Applied to biological tissue, the presented method could provide LC-OCT with the ability to quantify the scattering properties of tissue imaged *in vivo*, complementary to the qualitative information provided by the high-resolution of images. Potentially, the method could be used *in vivo* to characterize biological tissues and monitor structural changes that occur during the development of a pathology.

*Acknowledgments.* The authors would like to thank Pr. Audrey K. Bowden for the valuable and relevant discussion on the models allowing the measurement of optical properties in OCT. The authors also wish to thank PhD student Marc Chammas for his help in performing measurements using integrating spheres and collimated transmission set-up. They are also grateful to the whole team of engineers at DAMAE Medical for technical support.

## References

- 1 Dubois A., Levecq O., Azimani H., Davis A., Ogien J., Siret D., Barut A. (2018) Line-field confocal time domain optical coherence tomography with dynamic focusing, *Opt. Exp.* **26**, 33534.
- 2 Dubois A., Levecq O., Azimani H., Siret D., Barut A., Suppa M., del Marmol V., Malvey J., Cinotti E., Rubegni P., Perrot J.-L. (2018) Line-field confocal optical coherence tomography for high-resolution noninvasive imaging of skin tumors, *J. Biomed. Opt.* **23**, 1.
- 3 Ogien J., Daures A., Cazalas M., Perrot J.-L., Dubois A. (2020) Line-field confocal optical coherence tomography for three-dimensional skin imaging, *Front. Optoelectron.* **13**, 381–392.
- 4 Ogien J., Levecq O., Azimani H., Dubois A. (2020) Dual-mode line-field confocal optical coherence tomography for ultrahigh-resolution vertical and horizontal section imaging of human skin *in vivo*, *Biomed. Opt. Exp.* **11**, 1327.
- 5 Monnier J., Tognetti L., Miyamoto M., Suppa M., Cinotti E., Fontaine M., Perez J., Orte Cano C., Yélamos O., Puig S., Dubois A., Rubegni P., Marmol V., Malvey J., Perrot J. (2020) *In vivo* characterization of healthy human skin with a novel, non-invasive imaging technique: line-field confocal optical coherence tomography, *J. Eur. Acad. Dermatol. Venereol.* **34**, 2914–2921.
- 6 Chauvel-Picard J., Bérot V., Tognetti L., Orte Cano C., Fontaine M., Lenoir C., Pérez-Anker J., Puig S., Dubois A., Forestier S., Monnier J., Jdid R., Cazorla G., Pedrazzani M., Sanchez A., Fischman S., Rubegni P., del Marmol V., Malvey J., Cinotti E., Perrot J.L., Suppa M. (2022) Line-field confocal optical coherence tomography as a tool for three-dimensional *in vivo* quantification of healthy epidermis: a pilot study, *J. Biophotonics* **15**, e202100236.
- 7 Dejonckheere G., Suppa M., Marmol V., Meyer T., Stockfleth E. (2019) The actinic dysplasia syndrome – diagnostic approaches defining a new concept in field carcinogenesis with multiple cSCC, *J. Eur. Acad. Dermatol. Venereol.* **33**, 16–20.
- 8 Suppa M., Fontaine M., Dejonckheere G., Cinotti E., Yélamos O., Diet G., Tognetti L., Miyamoto M., Orte Cano C., Perez-Anker J., Panagiotou V., Trepant A., Monnier J., Berot V., Puig S., Rubegni P., Malvey J., Perrot J., Marmol V. (2021) Line-field confocal optical coherence tomography of basal cell carcinoma: a descriptive study, *J. Eur. Acad. Dermatol. Venereol.* **35**, 1099–1110.
- 9 Ruini C., Schuh S., Sattler E., Welzel J. (2021) Line-field confocal optical coherence tomography—practical applications in dermatology and comparison with established imaging methods, *Skin Res. Technol.* **27**, 340–352.
- 10 Cinotti E., Tognetti L., Cartocci A., Lamberti A., Gherbassi S., Orte Cano C., Lenoir C., Dejonckheere G., Diet G., Fontaine M., Miyamoto M., Perez-Anker J., Solmi V., Malvey J., Marmol V., Perrot J.L., Rubegni P., Suppa M. (2021) Line-field confocal optical coherence tomography for actinic keratosis and squamous cell carcinoma: a descriptive study, *Clin. Exp. Dermatol.* **46**, 1530–1541.
- 11 Oliveira L.M.C., Tuchin V.V. (2019) The optical clearing method, in: *SpringerBriefs in Physics*, Springer International Publishing.
- 12 Chang S., Bowden A.K. (2019) Review of methods and applications of attenuation coefficient measurements with optical coherence tomography, *J. Biomed. Opt.* **24**, 090901.

- 13 Liu S. (2017) Tissue characterization with depth-resolved attenuation coefficient and backscatter term in intravascular optical coherence tomography images, *J. Biomed. Opt.* **22**, 096004.
- 14 Kut C., Chaichana K.L., Xi J., Raza S.M., Ye X., McVeigh E.R., Rodriguez F.J., Quiñones-Hinojosa A., Li X. (2015) Detection of human brain cancer infiltration ex vivo and in vivo using quantitative optical coherence tomography, *Sci. Transl. Med.* **7**, 292ra100.
- 15 Vermeer K.A., van der Schoot J., Lemij H.G., de Boer J.F. (2012) Quantitative RNFL attenuation coefficient measurements by RPE-normalized OCT data, in: Manns F., Söderberg P.G., Ho A. (eds), *Ophthalmic Technologies XXII*, Vol. **8209**, SPIE, pp. 79–84.
- 16 Bus M., de Bruin D., Faber D., Kamphuis G., Zondervan P., Laguna-Pes M., van Leeuwen T., de Reijke T.M., de la Rosette J. (2016) Optical coherence tomography as a tool for in vivo staging and grading of upper urinary tract urothelial carcinoma: a study of diagnostic accuracy, *J. Urol.* **196**, 1749–1755.
- 17 Boone M., Suppa M., Miyamoto M., Marneffe A., Jemec G., Del Marmol V. (2016) In vivo assessment of optical properties of basal cell carcinoma and differentiation of BCC subtypes by high-definition optical coherence tomography, *Biomed. Opt. Exp.* **7**, 2269.
- 18 Gong P., Almasian M., van Soest G., de Bruin D.M., van Leeuwen T.G., Sampson D.D., Faber D.J. (2020) Parametric imaging of attenuation by optical coherence tomography: review of models, methods, and clinical translation, *J. Biomed. Opt.* **25**, 1.
- 19 Vermeer K.A., Mo J., Weda J.J.A., Lemij H.G., de Boer J.F. (2014) Depth-resolved model-based reconstruction of attenuation coefficients in optical coherence tomography, *Biomed. Opt. Exp.* **5**, 322–337.
- 20 Gupta K., Shenoy M.R. (2018) Method to determine the anisotropy parameter  $g$  of a turbid medium, *Appl. Opt.* **57**, 7559.
- 21 Thrane L., Yura H.T., Andersen P.E. (2000) Analysis of optical coherence tomography systems based on the extended Huygens–Fresnel principle, *J. Opt. Soc. Am. A* **17**, 484–490.
- 22 Turani Z., Fatemizadeh E., Blumetti T., Daveluy S., Moraes A.F., Chen W., Mehregan D., Andersen P.E., Nasiriavanaki M. (2019) Optical radiomic signatures derived from optical coherence tomography images improve identification of melanoma, *Cancer Res.* **79**, 2021–2030.
- 23 Thrane L., Frosz M.H., Jørgensen T.M., Tycho A., Yura H. T., Andersen P.E. (2004) Extraction of optical scattering parameters and attenuation compensation in optical coherence tomography images of multilayered tissue structures, *Opt. Lett.* **29**, 1641–1643.
- 24 Jacques S.L. (2013) *Confocal laser scanning microscopy using scattering as the contrast mechanism*, Springer, New York.
- 25 Samatham R., Jacques S.L. (2009) Determine scattering coefficient and anisotropy of scattering of tissue phantoms using reflectance-mode confocal microscopy, in: Wax A., Backman V. (eds), *Biomedical Applications of Light Scattering III*, Vol. **7187**, SPIE, pp. 152–159.
- 26 Choudhury N., Jacques S.L. (2012) Extracting scattering coefficient and anisotropy factor of tissue using optical coherence tomography, in: Jansen E.D., Thomas R.J. (eds), *Optical Interactions with Tissue and Cells XXIII*, Vol. **8221**, SPIE, pp. 144–148.
- 27 Abi-Haidar D., Olivier T. (2009) Confocal reflectance and two-photon microscopy studies of a songbird skull for preparation of transcranial imaging, *J. Biomed. Opt.* **14**, 3, 034038.
- 28 Jacques S.L., Samatham R., Choudhury N., Fu Y., Levitz D. (2008) Measuring tissue optical properties in vivo using reflectance-mode confocal microscopy and OCT, in: *Biomedical Applications of Light Scattering II*, Vol. **6864**, SPIE, pp. 57–64.
- 29 Jacques S.L. (2013) Optical properties of biological tissues: a review, *Phys. Med. Biol.* **58**, R37–R61.
- 30 Tuchin V.V. (1997) Light scattering study of tissues, *Phys.-Uspekhi* **40**, 495–515.
- 31 Kono T., Yamada J. (2019) In vivo measurement of optical properties of human skin for 450–800 nm and 950–1600 nm wavelengths, *Int. J. Thermophys.* **40**, 1–14.
- 32 <https://www.neyco.fr/nos-produits/silicones-2/microfluidique-pdms/silicone-sylgard-184/sylgard-184>.
- 33 Schneider F., Draheim J., Kamberger R., Wallrabe U. (2009) Process and material properties of polydimethyl siloxane (PDMS) for optical MEMS, *Sens. Actuators A Phys.* **151**, 95–99.
- 34 Bodurov I., Vlaeva I., Viraneva A., Yovcheva T., Sainov S. (2016) Modified design of a laser refractometer, *Nanosci. Nanotechnol.* **16**, 31–33.
- 35 Ghosh G. (1999) Dispersion-equation coefficients for the refractive index and birefringence of calcite and quartz crystals, *Opt. Commun.* **163**, 1, 95–102.
- 36 Sarkar S., Gupta V., Kumar M., Schubert J., Probst P.T., Joseph J., König T.A. (2019) Hybridized guided-mode resonances via colloidal plasmonic self-assembled grating, *ACS Appl. Mater. Interf.* **11**, 14, 13752–13760. PMID: 30874424.
- 37 Siefke T., Kroker S., Pfeiffer K., Puffky O., Dietrich K., Franta D., Ohlídal I., Szeghalmi A., Kley E.-B., Tünnermann A. (2016) Materials pushing the application limits of wire grid polarizers further into the deep ultraviolet spectral range, *Adv. Opt. Mater.* **4**, 11, 1780–1786.
- 38 Beek J.F., Blokland P., Posthumus P., Aalders M., Pickering J.W., Sterenborg H.J.C.M., van Gemert M.J.C. (1997) In vitro double-integrating-sphere optical properties of tissues between 630 and 1064 nm, *Phys. Med. Biol.* **42**, 2255–2261.
- 39 Bashkatov A.N., Genina E.A., Kochubey V.I., Tuchin V.V. (2005) Optical properties of human skin, subcutaneous and mucous tissues in the wavelength range from 400 to 2000 nm, *J. Phys. D Appl. Phys.* **38**, 2543–2555.
- 40 Ionescu A.M., Cardona J.C., Garzón I., Oliveira A.C., Ghinea R., Alaminos M., Pérez M.M. (2015) Integrating-sphere measurements for determining optical properties of tissue-engineered oral mucosa, *J. Eur. Opt. Soc. Rapid Publ.* **10**, 15012.
- 41 ul Rehman A., Ahmad I., Qureshi S.A. (2020) Biomedical applications of integrating sphere: a review, *Photodiagnosis Photodyn. Ther.* **31**, 101712.
- 42 Pickering J.W., Prahl S.A., van Wieringen N., Beek J.F., Sterenborg H.J.C.M., van Gemert M.J.C. (1993) Double-integrating-sphere system for measuring the optical properties of tissue, *Appl. Opt.* **32**, 399–410.
- 43 Prahl S. (2011) Optical property measurements using the inverse adding doubling program, *Technical Report*. [https://www.researchgate.net/publication/254428856\\_Optical\\_Property\\_Measurements\\_Using\\_the\\_Inverse\\_Adding\\_Doubling\\_Program](https://www.researchgate.net/publication/254428856_Optical_Property_Measurements_Using_the_Inverse_Adding_Doubling_Program).

- 44 Carminati R., Schotland J.C. (2021) *Principles of scattering and transport of light*, Cambridge University Press.
- 45 L.V. Wang and Wang H.I. (2007) *Biomedical optics: principles and imaging*.
- 46 Faber D.J., van der Meer F.J., Aalders M.C.G., van Leeuwen T.G. (2004) Quantitative measurement of attenuation coefficients of weakly scattering media using optical coherence tomography, *Opt. Exp.* **12**, 4353.
- 47 Turchin I.V., Sergeeva E.A., Dolin L.S., Kamensky V.A., Shakhova N.M., Richards-Kortum R.R. (2005) Novel algorithm of processing optical coherence tomography images for differentiation of biological tissue pathologies, *J. Biomed. Opt.* **10**, 6, 064024.
- 48 Ghafaryasl B., Vermeer K., Kalkman J., Callewaert T., de Boer J., Vliet L.V. (2021) Attenuation coefficient estimation in fourier-domain oct of multi-layered phantoms, *Biomed. Opt. Exp.* **12**, 2744–2758.
- 49 Wilson B.C. (1995) *Measurement of tissue optical properties: methods and theories*, Springer, US.

## Appendix

### A. Absorption coefficient measurement

See [Figure A1](#).

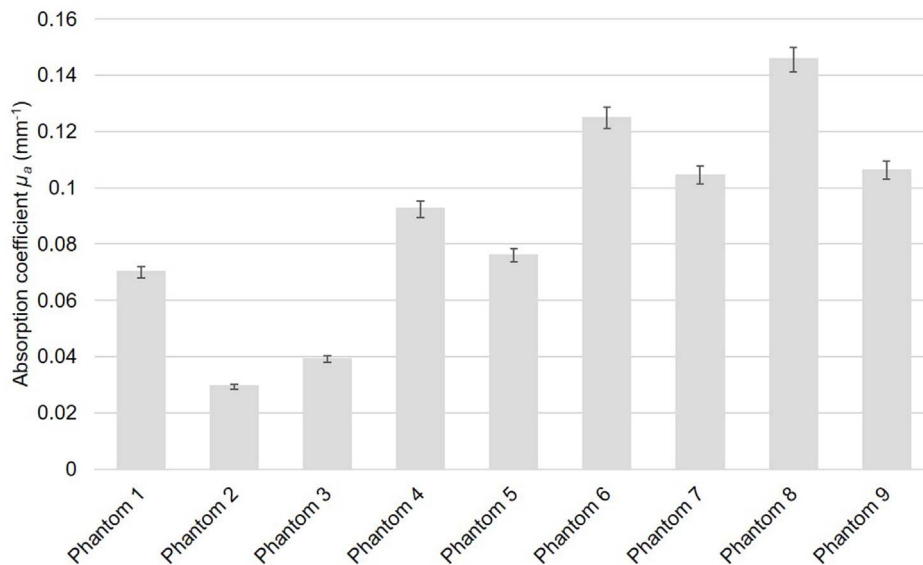


**Figure A1.** Values of  $\mu_a$  obtained at 785 nm from integrating spheres measurements for monolayered phantoms.